Optics Letters

Cross-polarized surface lattice resonances in a rectangular lattice plasmonic metasurface

M. Saad Bin-Alam,[1,*] Orad Reshef,[2] Raja Naeem Ahmad,[2,3] Jeremy Upham,[2] Mikko J. Huttunen,[4] Ksenia Dolgaleva,[1,2] and Robert W. Boyd[1,2,5]

[1]School of Electrical Engineering and Computer Science, University of Ottawa, Ottawa ON K1N 6N5, Canada
[2]Department of Physics, University of Ottawa, Ottawa ON K1N 6N5, Canada
[3]Max Plank Institute of Quantum Optics, Hans Kopfermann Str 1, 85748, Garching bei Munich, Germany
[4]Laboratory of Photonics, Tampere University, Tampere FI-33014, Finland
[5]The Institute of Optics and Department of Physics and Astronomy, University of Rochester, Rochester, New York 14627, USA
*Corresponding author: msaad009@uottawa.ca

Received 17 November 2021; revised 28 March 2022; accepted 30 March 2022; posted 31 March 2022; published 14 April 2022

Multiresonant metasurfaces could enable many applications in filtering, sensing, and nonlinear optics. However, developing a metasurface with more than one high-quality-factor or high-Q resonance at designated resonant wavelengths is challenging. Here, we experimentally demonstrate a plasmonic metasurface exhibiting different, narrow surface lattice resonances by exploiting the polarization degree of freedom where different lattice modes propagate along different dimensions of the lattice. The surface consists of aluminum nanostructures in a rectangular periodic lattice. The resulting surface lattice resonances were measured around 640 nm and 1160 nm with Q factors of ~50 and ~800, respectively. The latter is a record-high plasmonic Q factor within the near-infrared type-II window. Such metasurfaces could benefit such applications as frequency conversion and all-optical switching.

https://doi.org/10.1364/OL.448813

Resonant metasurfaces promise to enable free-space photonic applications in nanoscale thin flat optical devices [1]. Thanks to their strong resonance enhancement characteristics, plasmonic lattice metasurfaces formed by metal nanostructures are considered to be strong candidates for such applications as sensing, spectroscopy, and lasing [2–4]. Among those applications, some specific processes may involve two or more frequencies, particularly nonlinear optical processes, such as harmonic generation, frequency up- and downconversion, cross-phase modulation or ultrafast all-optical switching [5]. Strongly resonant responses, like plasmonic resonances, could boost the efficiency of nonlinear optical processes without requiring any phase-matching between the input and output waves [6,7]. Thus, an implementation of multiresonant plasmonic metasurfaces could dramatically enhance the efficiency of applications involving nonlinear optical phenomena [8].

Under optical illumination, metal nanostructures naturally exhibit strongly localized surface plasmon resonances (LSPRs) [9]. However, a longstanding issue with metal nanostructures is that of their high absorptive and radiative losses, which result in the swift decay of excitations associated with the LSPRs. Whereas absorptive losses are inherent to metals, it is possible to suppress the radiative or scattering losses by engineering periodic arrays of metal nanostructures to support plasmonic surface lattice resonances (SLRs) with longer lifetimes [4,10]. Such SLRs originate from the collective coupling of every particle in a lattice and suppress the scattered losses associated with the individual particles. Thus, the resulting resonances can have significantly high quality factors (Q>2000 [11]), appearing at the wavelength near the diffraction edge of the lattice periodicity. Under normal illumination, the spectral position of the SLRs can be defined by the product of the periodicity, P, of the particles toward its radiating direction and the refractive index n of the particles' surrounding background medium ($\lambda_{SLR} \approx nP$) [11,12].

As such, SLR modes are generated in the form of in-plane waves, oscillating orthogonally to the polarization direction of incident light. Hence, in a 2D plasmonic metasurface array with a rectangular lattice formation, it is possible to generate two different SLR modes along two separate orthogonal directions [13]. Such lattice modes, owing to orthogonally polarized incident waves, may be useful for linear applications, such as polarization-selective notch filters, or nonlinear optical processes, such as cross-phase modulation or two-beam coupling, which depend on more than one input field.

In this Letter, we report the observation of multiple LSPRs and SLRs at different wavelengths in the same metasurface. The resonant wavelengths of the SLRs can be selected through the careful choice of lattice geometry. The different resonances can be isolated by selecting a given linear polarization of the probing light or they can be excited simultaneously by employing diagonally polarized light.

To properly design a metasurface with multiple resonances in both the visible and infrared regime, here we consider the behavior of the constituent materials in the spectral range from 400 nm to 1300 nm. In noble plasmonic metals, like gold and silver, the interband transition occurs in the visible wavelength regime [14]. This transition causes such metals to absorb most of the visible light, and to lose their capability to support plasmon oscillations

in the shorter ultraviolet wavelength regime. However, unlike noble metals, the interband transition in aluminum appears in the near-infrared (NIR) regime (around $\lambda = 850$ nm). Furthermore, because of the electronic band structure of the aluminum, the interband transition is quite narrow [15]. Hence, aluminum retains its metallicity at shorter wavelengths, compared with gold or silver. Subsequently, aluminum nanostructures can exhibit LSPRs and can thus efficiently scatter light in the visible or ultraviolet spectral ranges [16]. Inspired by this fact, aluminum nanostructures have been recently adopted to demonstrate SLRs in periodic metasurfaces with applications in SHG and nanolasing [3,12,13]. It was also revealed that aluminum possesses a comparatively larger nonlinear optical coefficient than gold or silver [17,18]. We therefore elect to have our metasurface composed of aluminum nanoparticles cladded in a transparent, fused silica substrate.

Typically, the collective SLRs are excited at the longer wavelength tails of the LSPRs corresponding to the individual nanostructures [4]. As we aim to excite polarization-dependent SLRs, here we fabricate periodic right-angled V-shaped aluminum nanostructures, since this particular shape is used to exhibit two polarization-dependent LSPRs at different wavelengths [6,19,20]. The fabricated dimensions are: length $L \approx$ 110–130 nm; width $W \approx$ 70–80 nm; and thickness $t \approx 30$ nm. The overall array size is $400 \times 400\ \mu m^2$. This design was selected to serve as a proof of principle for this approach to a flexible multiresonant metasurface, exhibiting SLRs in the visible and NIR spectra with high Q factors. For conceptual clarity, we investigated a rectangular lattice, supporting two orthogonal SLRs, excited using either x- or y-polarized incident light at normal incidence to the surface. This design makes it straightforward to independently control the properties of the SLRs by adjusting the incident polarization and the tilting angles of the metasurface. For example, the center wavelengths of the SLR could be controlled by appropriately tilting the metasurface. However, we note that different particle geometries or oblique lattices might be beneficial for applications, such as nonlinear frequency conversion, where mode overlaps between several SLRs should be optimized.

Figures 1(a)–1(c) illustrate the designed metasurface in 2D. Here, we depict the LSPR by the glowing yellow ring encircling each V-shape nanostructure, the SLR mode for x-polarization in red vertically, and the SLR mode for y-polarization in green horizontally in Fig. 1(a) and 1(b), respectively. In Fig. 1(c), we show that both SLRs can be excited simultaneously using diagonally polarized illumination. A focused-ion beam micrograph of the fabricated array is depicted in Fig. 1(d). The periodic structured particles form a rectangular lattice in the xy plane (periodicity $P_x \approx 445$ nm and $P_y \approx 790$ nm) inside a fused silica substrate (refractive index $n = 1.46$).

The sample fabrication and the experimental technique are similar to those of Ref. [11]. We fabricate metasurfaces using a standard metal lift-off process. On top of a fused silica substrate, we deposit a silica undercladding layer using sputtering. Next, we define the pattern of the nanostructure arrays using electron-beam lithography in a positive tone resist bilayer with the help of a commercial conductive polymer. To correct for the nanostructure corner rounding, we design the mask using shape-correction proximity error correction. After the development, we deposit an aluminum layer using thermal evaporation followed by the lift-off process. We deposit a 200 nm thick final protective silica cladding layer using sputtering to protect the

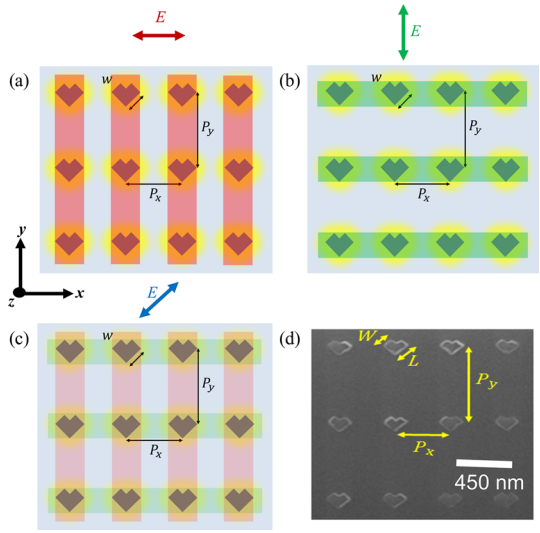

Fig. 1. Plasmonic metasurface in 2D. Normally incident light polarized (a) along the x-axis excites an SLR along the periodicity P_y (vertical, red), (b) along the y-axis excites an SLR along the periodicity P_x (horizontal, green), and (c) diagonally simultaneously excites SLRs along both directions. The yellow ring encircling each V-shaped nanostructure represents the LSPRs. (d) Focused-ion beam micrograph of fabricated metasurface.

aluminum nanoparticles from oxidization. To make sure that the environment surrounding the metasurface is completely homogeneous, we sputter the initial and final silica layers using the same tool under the same conditions. Before the characterization, we cover the surface of the device in index-matching oil and also coat the backside of the silica substrate with an antireflective coating to minimize substrate-related etalon fringes [21].

In the experiment, we use a normally incident collimated light beam from a broadband supercontinuum laser source (spectral range $\lambda = 470$–2400 nm) to flood-illuminate all of the metasurface arrays in the sample. We control the incident polarization using a broadband linear polarizing filter. We observe the image of the light transmitted by the metasurface using a lens with a focal length $f = 35$ mm and by placing a 100 μm pinhole in the image plane to collect the image of the desired array. We use a large-core (400 μm) multimode fiber to collect the transmitted light from the sample metasurface array and pass it to an optical spectrum analyzer (OSA). The resolution of the OSA is set to 0.01 nm. The OSA is used to measure the transmittance spectra by taking the ratio of light transmitted through the aluminum nanostructured metasurface array to light transmitted through the substrate without the metasurface array.

Figure 2(a) shows the simulated transmission spectra of our designed metasurface for different polarization states. The finite-difference time domain (FDTD) simulation was performed using Lumerical FDTD software. We also measured the normalized transmission spectra of our fabricated metasurface, illuminating it with a normally incident collimated beam generated from a broadband supercontinuum source. Figure 2(b) shows the measured normalized transmission spectra for different polarization states; these are in good agreement with the simulated results, shown in Fig. 2(a). For convenience, the resonances in the visible and infrared are presented separately in Figs. 2(c)–2(h) for different polarization states. It is evident in the enlarged spectra that, in the visible regime, the x-polarized

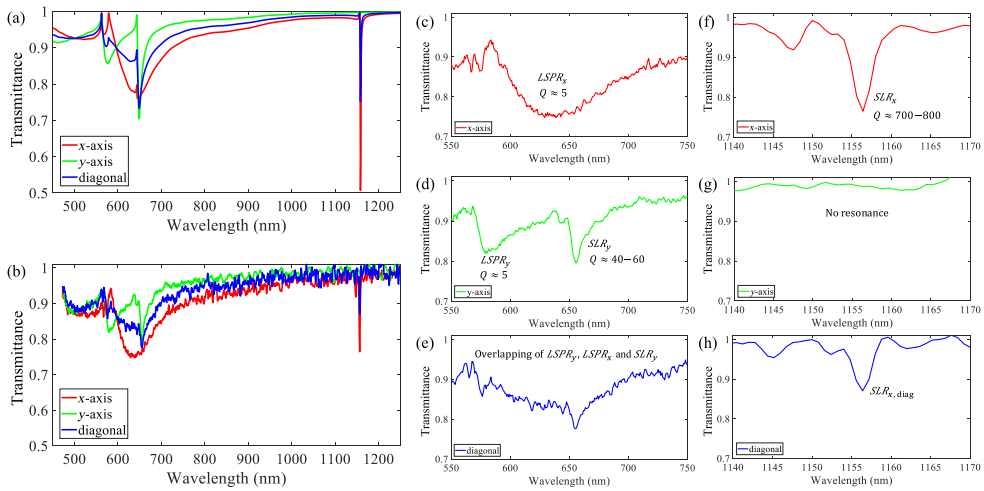

Fig. 2. (a) Simulated and (b) experimentally measured normalized transmission spectra of the polarization-dependent (*x*-axis, *y*-axis, and diagonal) multiresonant LSPRs and SLRs in the plasmonic metasurface. Diagonally polarized light excites the LSPRs and SLRs of both dimensions, enabling simultaneous SLRs around 649 nm and 1150 nm. (c)–(h) Close-ups of the measured spectra for the (c)–(e) visible and (f)–(h) NIR resonances for different polarizations.

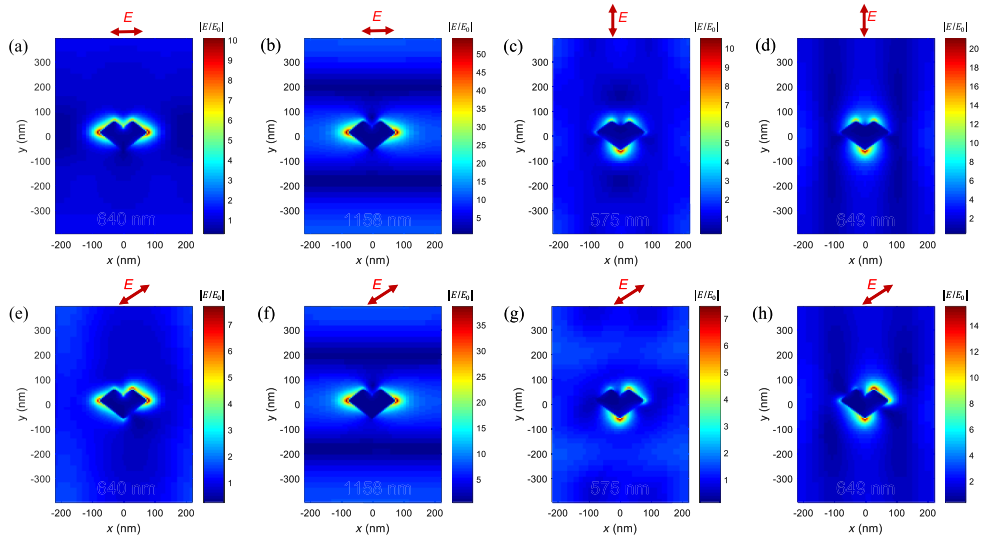

Fig. 3. Normalized electric field distributions of the SLR modes for the *x*-polarization at (a) 640 nm and (b) 1158 nm, *y*-polarization at (c) 575 nm and (d) 649 nm, and diagonal polarization at (e) 640 nm, (f) 1158 nm, (g) 575 nm, and (h) 649 nm.

LSPR [Fig. 2(c)] overlaps with the *y*-polarized LSPR and SLR [Fig. 2(d)] under diagonally polarized excitation [Fig. 2(e)]. We note that the resonance strength is halved from its original value, as conceptually predicted in Fig. 1(c) and simulated in Fig. 2(a). Such overlapping causes the resonances in the visible regime to superimpose with each other and thus form a modified spectral line shape, as depicted in Fig. 2(e). The Q factors of the LSPRs for both the *x*- and *y*-polarization are around 5, whereas the SLR Q factor for the *y*-polarization is around 50.

As expected, the SLR for the *x*-polarization in the infrared regime [shown in Fig. 2(f)] emerged at the far spectral distance, redshifted from all other resonance features in the visible regime. From different samples of our designed metasurface, we find the Q value for this infrared SLR to vary between 700 and 820. Although the high-Q SLR feature completely vanishes under *y*-polarized excitation [see Fig. 2(g)], it can emerge without any spectral modification for any other polarization states with reduced strength. Thus, as expected, we observe the re-appearance of the high-Q SLR in Fig. 2(h) for the diagonal polarization.

Next, we investigated the impact of the polarization state rotation on the in-plane electric field distribution inside the metasurface for all the resonances we discussed previously (Fig. 3). The simulated normalized electric field distribution corresponding to the LSPR around $\lambda = 629$ nm is presented in Fig. 3(a) and the SLR around 1158 nm is presented in Fig. 3(b) for the *x*-polarization. These figures show that the horizontally excited LSPR mode is only localized near the individual nanostructures; however, the delocalized SLR mode forms a delocalized diffraction grating-like standing wave, extended along the *y*-axis orthogonal to the polarization direction, which is in keeping with previous investigations of such lattice modes [12]. The electric field strength of the SLR is significantly higher than that of its

LSPR counterpart, as indicated by the color bars in Figs. 3(a) and 3(b), respectively. Such a large field enhancement in the SLR is the outcome of the scattering loss reduction by trapping the energy of scattered light near the diffraction order. The field distributions for these modes under *y*-polarized illumination are presented in Figs. 3(c) and 3(d). These modes are similar to their *x*-polarized counterparts, except that they are pointed along the *y*-direction, and feature smaller field enhancements, owing to a lower value of the associated Q factor.

We now turn to the electric field distribution under diagonal polarization. The fields in Fig. 3(e) depict the LSPR field under diagonally polarized light at 640 nm. Here, an SLR-like grating mode can be observed forming along the edges of the unit cell. This SLR-like feature around the LSPR center wavelength stems from the *y*-polarized SLR mode at 649 nm [Fig. 3(d)]. This indicates that, under diagonally polarized light, the *x*-polarized LSPR and the *y*-polarized SLR are superimposed. Comparing the scales between Fig. 3(a) and Fig. 3(e),we see that the overall field strength of the original LSPR for the *x*-polarization is slightly reduced in this superimposed mode by the off-axis diagonal polarization state.

In contrast, Fig. 3(f) shows no deviation of the stand-alone high-Q SLR field distribution around 1158 nm for the diagonal polarization from its *x*-polarization counterpart in Fig. 3(b), except the reduction of the field strength values indicated by the color bars. This feature confirms the behavior previously observed in Fig. 2(h), which depicts no spectral modification of the sharp infrared SLR in Fig. 2(f), owing to the lack of any other resonance nearby in Fig. 2(g). Next, we see that the LSPR field distribution for the *y*-polarization around 575 nm in Fig. 3(c) is also modified by the diagonally polarized light in Fig. 3(g). Such a modification occurs because of the superimposing of this LSPR for the *y*-polarization around 575 nm with the LSPR for the *x*-polarization around 640 nm. Contrary to the LSPR around 640 nm, this short wavelength modified LSPR around 575 nm is positioned relatively far from the SLR around 649 nm. Thus, the corresponding field distribution in Fig. 3(g) does not show a pronounced SLR-like grating.

Lastly, the field distribution in Fig. 3(h) depicts an SLR-like field distribution, just as in Fig. 3(d). These observations suggest that the field distribution of the localized, plasmon-like modes are dictated by polarization, whereas the SLR mode is dictated by the excitation wavelength.

In summary, we have experimentally demonstrated a technique to simultaneously excite cross-polarized dual LSPR and SLR modes in a nanostructured periodic metasurface via diagonally polarized normally incident light. The two different orthogonal SLRs, at wavelengths λ =649 nm and λ =1158 nm, could be tuned independently by modifying P_x and P_y, respectively. These two SLRs can be excited simultaneously using diagonally polarized light. We observed an unprecedentedly large Q factor for the SLR in the infrared type-II regime ($Q \approx 800$ around λ =1158 nm) and analyzed the resonance characteristics and relevant electric field distribution of the generated modes. The Q factor of the SLRs in the visible region could probably be further enhanced by tuning dimensions and periodicity and enlarging the metasurface area [11,13]. In addition, because this approach to a multiresonant metasurface is independent of multiresonances demonstrated elsewhere [21], they could probably be combined to design particular mode coupling or even hybridized modes. This multiresonant high-Q metasurface is a proof of principle for efficient, polarization-selective filtering. Nonlinear optical processes in flat photonic devices, such as SHG to photon-pair generation via spontaneous parametric downconversion, may also be possible.

Acknowledgments. The authors thank Iridian Spectral Technologies Ltd, Ottawa, ON, Canada, for help in cladding the silica superstrate on top of the metasurface substrate for this work.

Disclosures. The authors declare no conflicts of interest.

Data availability. Data underlying the results presented in this paper are not publicly available at this time but may be obtained from the authors upon reasonable request.

REFERENCES

1. A. V. Kildishev, A. Boltasseva, and V. M. Shalaev, Science **339**, 1232009 (2013).
2. B. Špačková, P. Wrobel, M. Bocková, and J. Homola, Proc. IEEE **104**, 2380 (2016).
3. D. Wang, J. Guan, J. Hu, M. R. Bourgeois, and T. W. Odom, Acc. Chem. Res. **52**, 2997 (2019).
4. V. G. Kravets, A. V. Kabashin, W. L. Barnes, and A. N. Grigorenko, Chem. Rev. **118**, 5912 (2018).
5. R. W. Boyd, *Nonlinear Optics* (Academic, 2020).
6. M. Kauranen and A. V. Zayats, Nat. Photonics **6**, 737 (2012).
7. M. S. Bin-Alam, J. Baxter, K. M. Awan, A. Kiviniemi, Y. Mamchur, A. C. Lesina, K. L. Tsakmakidis, M. J. Huttunen, L. Ramunno, and K. Dolgaleva, Nano Lett. **21**, 51 (2021).
8. J. Butet, P.-F. Brevet, and O. J. F. Martin, ACS Nano **9**, 10545 (2015).
9. N. Meinzer, W. L. Barnes, and I. R. Hooper, Nat. Photonics **8**, 889 (2014).
10. C. Cherqui, M. R. Bourgeois, D. Wang, and G. C. Schatz, Acc. Chem. Res. **52**, 2548 (2019).
11. M. S. Bin-Alam, O. Reshef, Y. Mamchur, M. Z. Alam, G. Carlow, J. Upham, B. T. Sullivan, J.-M. Ménard, M. J. Huttunen, R. W. Boyd, and K. Dolgaleva, Nat. Commun. **12**, 974 (2021).
12. D. Khlopin, F. Laux, W. P. Wardley, J. Martin, G. A. Wurtz, J. Plain, N. Bonod, A. V. Zayats, W. Dickson, and D. Gérard, J. Opt. Soc. Am. B **34**, 691 (2017).
13. M. J. Huttunen, O. Reshef, T. Stolt, K. Dolgaleva, and R. W. Boyd, J. Opt. Soc. Am. B **36**, E30 (2019).
14. S. A. Maier, *Plasmonics: Fundamentals and applications* (Springer, 2007).
15. D. Gérard and S. K. Gray, J. Phys. D: Appl. Phys. **48**, 184001 (2015).
16. M. W. Knight, N. S. King, L. Liu, H. O. Everitt, P. Nordlander, and N. J. Halas, ACS Nano **8**, 834 (2014).
17. B. Metzger, L. Gui, J. Fuchs, D. Floess, M. Hentschel, and H. Giessen, Nano Lett. **15**, 3917 (2015).
18. M. Castro-Lopez, D. Brinks, R. Sapienza, and N. F. van Hulst, Nano Lett. **11**, 4674 (2011).
19. M. Celebrano, X. Wu, M. Baselli, S. Großmann, P. Biagioni, A. Locatelli, C De Angelis, G. Cerullo, R. Osellame, B. Hecht, L. Duò, F. Ciccacci, and M. Finazzi, Nat. Nanotechnol. **10**, 412 (2015).
20. R. Czaplicki, A. Kiviniemi, M. J. Huttunen, X. Zang, T. Stolt, I. Vartiainen, J. Butet, M. Kuittinen, O. J. F. Martin, and M. Kauranen, Nano Lett. **18**, 7709 (2018).
21. O. Reshef, M. Saad-Bin-Alam, M. J. Huttunen, G. Carlow, B. T. Sullivan, J.-M. Ménard, K. Dolgaleva, and R. W. Boyd, Nano Lett. **19**, 6429 (2019).